Earth and Planetary Science Letters 510 (2019) 153–160

Contents lists available at ScienceDirect

Earth and Planetary Science Letters

www.elsevier.com/locate/epsl

First-principles calculations of equilibrium Ca isotope fractionation: Implications for oldhamite formation and evolution of lunar magma ocean

Fang Huang [a,*], Chen Zhou [a], Wenzhong Wang [b], Jinting Kang [a], Zhongqing Wu [b,*]

[a] CAS Key Laboratory of Crust–Mantle Materials and Environments, School of Earth and Space Sciences, University of Science and Technology of China, Hefei, Anhui 230026, China

[b] Laboratory of Seismology and Physics of Earth's Interior, School of Earth and Space Sciences, University of Science and Technology of China, Hefei, Anhui 230026, China

ARTICLE INFO

Article history:
Received 25 July 2018
Received in revised form 25 December 2018
Accepted 26 December 2018
Available online xxxx
Editor: F. Moynier

Keywords:
Ca isotopes
first-principles calculation
equilibrium isotope fractionation
oldhamite
lunar magma ocean

ABSTRACT

Calcium is a major element of the Earth, the Moon, terrestrial planets, and rocky meteorites. Here we present equilibrium Ca isotope fractionation factors of Ca-bearing minerals using the first-principles calculations based on density functional theory (DFT). The sequence of minerals from the isotopically heaviest to the lightest in Ca is forsterite > orthopyroxene (opx) > grossular ~ pigeonite > diopside > anorthite > oldhamite. Overall, the equilibrium fractionation of Ca isotopes is mainly controlled by the average bond lengths. Although oldhamite is enriched in light Ca isotopes relative to silicate minerals in equilibrium, natural oldhamite of enstatite chondrites are isotopically heavier than coexisting silicate materials. This implies that enstatite chondrites oldhamites should have been formed during solar nebular gas condensation instead than during parent body processing.

Following previous models for crystallization of the Lunar Magma Ocean (LMO), we simulated Ca isotopic fractionation of the LMO based on our calculated equilibrium Ca isotope fractionation factors. It shows that the $\delta^{44/40}$Ca of the lunar anorthositic crust should be lower than the average of the bulk Moon by 0.09–0.11‰. Considering that the lunar mantle might have overturned and mixed after solidification of the LMO, we further predict that the lunar mantle should be isotopically heavier than the bulk Moon by 0.17–0.26‰ if the mantle was fully overturned, or only by 0.06–0.08‰ for the case of fully mixing. Therefore, we predict that the potential offset of Ca isotopic composition between the anorthositic crust and the lunar mantle can be used to test LMO evolution models.

1. Introduction

Calcium is the sixth most abundant element of the Earth and has six stable isotopes (^{40}Ca, ^{42}Ca, ^{43}Ca, ^{44}Ca, ^{46}Ca, and ^{48}Ca). The relative mass-difference between ^{40}Ca and ^{48}Ca is the largest among isotopes of elements of the periodic table at the exception of H and He. Because Ca has a high 50% condensation temperature of 1505–1517 K (Lodders, 2003), a highly lithophile affinity, and a single valence state, its isotopes show a great potential in investigating high-temperature geochemical and cosmochemical processes such as the formation and evolution of the terrestrial planets and the genetic relationships among meteorites, Earth, Moon, and Mars (e.g., Simon and DePaolo, 2010; Valdes et al., 2014; Magna et al., 2015; Huang and Jacobsen, 2017; Amsellem et al., 2017; Simon et al., 2017; Kang et al., 2016, 2017; Zhao et al., 2017).

Knowledge of Ca isotopic compositions of different chondrites is the premise of using Ca isotopes as a geochemical tracer. Previous studies have measured mass-dependent Ca isotopic compositions in enstatite chondrites, ordinary chondrites, and carbonaceous chondrites to explore the chemical heterogeneity of meteorites, planets, and protoplanetary disk (Simon and DePaolo, 2010; Valdes et al., 2014; Huang and Jacobsen, 2017; Amsellem et al., 2017). A special attention has been given to enstatite chondrites since they are usually the isotopically closest meteorites to the Earth and have been proposed as candidates for the building blocks of the Earth (e.g., Javoy et al., 2010). However, there is still discrepancy on the Ca isotopic compositions of enstatite chondrites measured by different labs. For example, Simon and DePaolo (2010) found that enstatite chondrites are enriched in heavy Ca isotopes relative to the Earth by 0.16 to 0.51‰, while

* Corresponding authors.
E-mail addresses: fhuang@ustc.edu.cn (F. Huang), wuzq10@ustc.edu.cn (Z. Wu).

https://doi.org/10.1016/j.epsl.2018.12.034
0012-821X/

Valdes et al. (2014) and Huang and Jacobsen (2017) have documented that enstatite chondrites are isotopically identical to the bulk silicate Earth (BSE). Valdes et al. (2014) suggested the possible reason for this disagreement is that the dominant Ca-bearing minerals in enstatite chondrites (such as CaS, oldhamite) are isotopically different from other Ca-bearing minerals (such as anorthite and diopside), which sheds important light on the origin and differentiation of enstatite chondrites. There is however no theoretical information on how Ca isotopes behave between oldhamite and other Ca-bearing minerals. Therefore, to better understand how the main Ca-bearing minerals formed in enstatite chondrites using Ca isotopic data, it is critical to investigate the equilibrium Ca isotope fractionation factors among major Ca-bearing minerals in meteorites.

Calcium isotope compositions of rock and mineral samples can also be used to constrain the formation and evolution of the Earth and Moon. Calcium is a major element in clinopyroxene (cpx), anorthite, amphibole, garnet, pigeonite (~3 wt%) and Ca-perovskite, a minor element in orthopyroxene (opx, ~0.5 wt%), and a trace element in olivine (<0.1 wt%) and spinel (<0.1 wt%). Previous studies revealed up to ~1‰ offset of $\delta^{44/40}$Ca (defined as $[(^{44}Ca/^{40}Ca)_{sample}/(^{44}Ca/^{40}Ca)_{SRM915a} - 1] * 1000‰$) between co-existing opx and cpx in peridotites (Huang et al., 2010; Kang et al., 2016). Based on the measurements of fertile peridotites, Kang et al. (2017) estimated that the average $\delta^{44/40}$Ca of the upper mantle was 0.94 ± 0.05‰ (relative to SRM915a), slightly lower than the value estimated from cpx and opx data in Huang et al. (2010). Anorthosites and basalts in the lunar crust were considered to originate from the crystallization and segregation of plagioclase, olivine, opx, and cpx during the solidification of the lunar magma ocean (LMO) (e.g., Snyder et al., 1992; Norman et al., 2003; Elkins-Tanton et al., 2011). Although Ca isotope data for lunar samples are scarce (Simon and DePaolo, 2010; Valdes et al., 2014; Huang and Jacobsen, 2017; Simon et al., 2017), equilibrium fractionation factors of Ca isotopes among major Ca-bearing minerals are important for future Ca isotopic studies on the LMO processes.

Experimental calibration of inter-mineral equilibrium isotope fractionation at high temperature is still challenging because of the uncertainty and difficulty to reach the thermodynamic equilibrium among minerals. No high temperature experimental data for Ca has been reported in the literature. With recent advances in the computational capability, the first-principles calculations, which are based on the density functional theory (DFT), have been widely used to estimate equilibrium isotope fractionation factors for many stable isotope systems including Mg, Si, Ca, Fe, Ni, Cu, Zn (e.g., Fujii et al., 2011, 2014; Schauble, 2011; Huang et al., 2014; Ducher et al., 2016; Wang et al., 2017a; Moynier and Fujii, 2017). The DFT method can provide reliable data for mineral structure with the precision comparable to experimental studies (Lajaeghere et al., 2016), which can be further applied to accurately calculate isotope fractionation factors.

Recently, Feng et al. (2014) and Wang et al. (2017b) calculated the equilibrium Ca isotope fractionation factors between opx and cpx, which is dependent on Ca/Mg of opx. However, Ca isotope equilibrium fractionation factors among most other Ca-bearing minerals, including those common in the meteorites, the crust and mantle of the Earth and Moon, have not been investigated. Here we calculate equilibrium fractionation factors of Ca isotopes using the first-principles calculations based on the DFT method. The major Ca-bearing minerals investigated in this study include anorthite, forsterite, grossular, pigeonite, and oldhamite. This study provides an important dataset for equilibrium Ca isotope fractionation among common Ca-bearing minerals and explores the controlling factors on the Ca isotope fractionation from the perspective of crystal chemistry. Furthermore, we explore the formation of oldhamite in enstatite chondrites and predict the possible Ca isotopic fractionation between the anorthositic crust and the lunar mantle to constrain the solidification process of the LMO.

2. Methods

2.1. Equilibrium isotope fractionation factor

The isotope fractionation factor of an element X between mineral A and B, α_{A-B}, is defined as the ratio of their isotope ratios. α_{A-B} is related to the equilibrium constants of isotopic exchange reactions which can be derived from statistical physics and quantum mechanics with a series of approximations when it comes to gaseous reactions (Urey, 1947; Bigeleisen and Mayer, 1947) and minerals (Schauble, 2004). With regard to element X in crystal A, we can define a function β_A which is called reduced partition function ratio (RPFR), identical to the isotope fractionation factor between the phase A and the ideal gas of X atoms. β_A can be written as:

$$\beta_A = \prod_{i=1}^{3N-3} \frac{u_{i,h}}{u_{i,l}} \frac{e^{-\frac{1}{2}u_{i,h}}}{1-e^{-u_{i,h}}} \frac{1-e^{-u_{i,l}}}{e^{-\frac{1}{2}u_{i,l}}} \quad (1)$$

where $u_{i,h} = \frac{h_p \nu_{i,h}}{k_b T}$, $\nu_{i,h}$ is the vibrational frequency and i represents the ith vibrational mode, N is the number of atoms in the unit cell, h and l refer to the heavy and light isotopes, respectively. Parameter h_p is the Planck's constant, k_b is the Boltzmann's constant, and T is temperature in Kelvin. According to the definition of equilibrium fractionation factor, $\alpha_{A-B} = \beta_A/\beta_B$, where β_B is defined equally to β_A.

2.2. DFT calculations

The β factors of minerals can be calculated using Eq. (1) based on the vibrational frequencies obtained from the first-principles calculations. The electronic structure calculations were performed with the Quantum ESPRESSO, an open source software package based on the DFT, plane wave, and pseudopotential method (Giannozzi et al., 2009). The type of exchange correlation functional used here is local density approximation (LDA) (Perdew and Zunger, 1981) because the LDA has been proved to provide reliable vibrational frequencies of minerals as discussed in previous studies (Huang et al., 2013, 2014; Feng et al., 2014).

The pseudopotentials for O, Mg, Al, Si, and Ca used in this study are the same as those used in Huang et al. (2013). The pseudopotential for S was generated by Vanderbilt method (Vanderbilt, 1990) with the valence configuration $3s^2 3p^4$ and the cutoff radii of 1.70 Bohr. The plane-wave energy cutoffs were set to 70 Ry. Brillouin zone summations over electronic states were performed over $N_1 \times N_2 \times N_3$ k-mesh with N_i dependence on the materials (see Table S1). Each structure was optimized using variable cell shape molecular dynamics (Wentzcovitch, 1991) until residual forces acting on every atom were less than 1×10^{-4} Ry/Bohr and unit-cell stresses were less than 0.5 kbar. Dynamical matrices were computed on regular q-mesh using the density functional perturbation theory (DFPT) (Baroni et al., 2001) and then interpolated in a dense q-mesh to obtain the vibrational density of state (VDoS) of minerals (Table S1). Therefore, their RPFRs can be derived from vibrational frequencies. For minerals with more than 150 atoms, because the calculations of VDoS based on the DFPT require extremely huge computations, the RPFRs were obtained from force constants calculated by the small displacement (0.02 Å, 0.04 Å, and 0.06 Å from equilibrium position) method (Schauble, 2011) based on the high-temperature approximation (Bigeleisen and Mayer, 1947).

3. Results

3.1. Crystal structures and vibrational properties

The initial crystal structures of anorthite, forsterite, grossular, oldhamite, and pigeonite are available in American Mineralogist Crystal Structure Database (AMCSD). Calcium is a trace or minor element in forsterite and pigeonite, which both have two non-equivalent Mg sites (M_1 and M_2). Magnesium atoms in forsterite and pigeonite can be replaced by Ca atoms to form Ca-doped structures. Our calculations show that Ca prefers to occupy the M_2 site relative to the M_1 site in forsterite and pigeonite. Thus, the case that Ca atom is incorporated into the M_2 site was taken into account in this study. Ideal primitive cells of forsterite and pigeonite contain 28 and 40 atoms, respectively. The initial Ca-bearing structures of forsterite with the CaO content of 2.48 wt.% and 1.25 wt.% were generated by substituting one M_2-site Mg atom with one Ca atom in the 112-atom and 224-atom supercells of forsterite, respectively. The 112-atom supercell was constructed by expanding the primitive cell of forsterite twice along both of a and c directions. Similarly, we separately expanded the primitive cell twice along a, b, and c directions to obtain the 224-atom one. For Ca-bearing pigeonite, we expanded the primitive cell twice along b and c directions to obtain the 160-atom supercell, and considered three different CaO contents (6.86 wt.%, 3.47 wt.%, and 1.74 wt.%). The initial structures with 6.86 wt.% and 1.74 wt.% CaO were obtained by substituting one M_2-site Mg atom with one Ca atom in its primitive cell and 160-atom supercell; the one with the CaO content of 3.47 wt.% was generated by substituting two M_2-site Mg atoms with two Ca atoms in the 160-atom supercell. Because there is more than one configuration for the initial structures of pigeonite with 3.4 wt.% CaO, all nonequivalent configurations were calculated and the configuration with the lowest total energy was selected for the $10^3 \ln\beta$ calculations.

The relaxed crystal structures of anorthite, grossular, oldhamite, pigeonite, and forsterite are shown in Fig. S1 and the relaxed cell parameters and volumes of these minerals at static conditions are compared with experimental measurements at ambient conditions in Table S2. Because the effects of zero-point motion and temperature are not considered in this study, the calculated results are slightly underestimated relative to the experimental data, which is typical for the LDA calculations (Wentzcovitch et al., 2010; Feng et al., 2014; Wang et al., 2017a, 2017b). Notably, our previous studies (Huang et al., 2013, 2014) have clearly demonstrated that, after accounting for the contributions of zero-point motion and temperature, the calculated volumes of minerals within the LDA at ambient conditions agree well with experimental results. Moreover, the distributions of the theoretical and experimental Ca–O/S bond lengths in anorthite, grossular, and oldhamite agree well with each other, indicating that relaxed crystal structures are reliable (Fig. S2). The underestimation of volume in this study may lead to significant variations in $10^3 \ln\beta$, but this does not significantly affect $10^3 \ln\alpha$ among minerals because the systematic offsets of $10^3 \ln\beta$ can be canceled out. This is also strongly supported by previous theoretical results that the LDA and the generalized gradient approximation (GGA) predict similar $10^3 \ln\alpha$ of Mg and Si isotopes among minerals (Méheut et al., 2009; Schauble, 2011; Huang et al., 2013; Méheut and Schauble, 2014; Qin et al., 2016), although the volume is slightly underestimated by the LDA and overestimated by the GGA (Wentzcovitch et al., 2010).

The comparison of calculated frequencies with experimental data are presented in Fig. 1 and Table S4. Our calculated results agree well with experimental measurements for grossular with the slope between calculated frequencies and measured frequencies being 1.002 ± 0.002 (1σ, $R^2 = 0.9996$). For oldhamite, the lower frequency obtained from calculation significantly deviates from the experimental one (240 cm^{-1} vs 285 cm^{-1}) whereas the higher frequencies from calculation and experiment are identical (349 cm^{-1} vs 350 cm^{-1}). All the frequencies in an ideally ordered oldhamite are infrared-active but inactive in Raman according to the group theory. However, the experimental frequencies in Avril et al. (2013) are identified by Raman spectroscopy. Avril et al. (2013) mentioned that the Raman frequencies were activated by local symmetry breaking. The vibrational frequencies might be shifted in this process. Except for the lower frequency in oldhamite, our calculated frequencies well match the experimental results, which demonstrates the reliability and accuracy of the calculated equilibrium isotope fractionation factors. Because $10^3 \ln\beta$ is proportional to the square of the scale factor at high temperature and is positively correlated to the scale factor at low temperature (Bigeleisen and Mayer, 1947; Méheut et al., 2009; Cao and Liu, 2011), the uncertainties of our calculated $10^3 \ln\beta$ and $10^3 \ln\alpha$ are less than 0.5% and 1%, respectively, in relative deviation. Specifically, the calculated $10^3 \ln\alpha$ of $^{18}O/^{16}O$ among minerals in this study agree well with the experimental calibrations at equilibrium (Fig. S3 and Table S5), further demonstrating the reliability of our calculations.

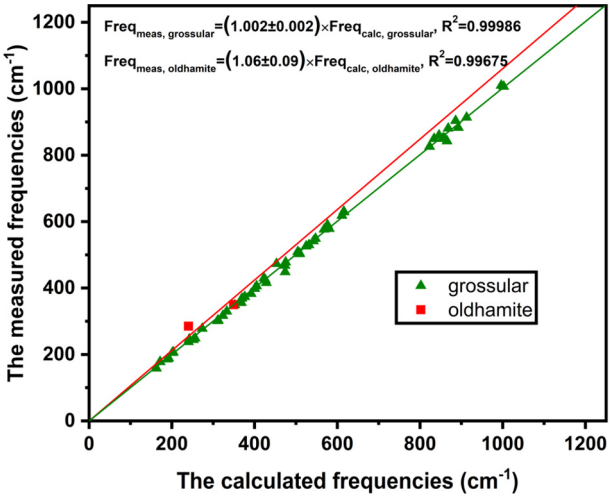

Fig. 1. Comparison of the calculated frequencies with the measured values (data are in Table S3).

3.2. Average bond lengths

Bond lengths of Ca–O/S in calculated minerals as well as their coordination numbers (CN) are reported in Table 1 and Table S3. Our calculations show that Ca is 6-fold coordinated in forsterite and oldhamite, and 7-fold coordinated in pigeonite. For anorthite, there are four different Ca atoms with 6, 7, 7, and 7-fold coordination, respectively; the average CN of Ca is 6.75. In addition, the CN of Ca in grossular is 8. The average lengths of Ca–O bonds in the investigated minerals range from 2.269 Å to 2.470 Å (Table 1), while the average Ca–S bond length in oldhamite is 2.826 Å. Average Ca–O bond lengths in forsterite with 2.48 wt.% to 1.25 wt.% CaO content are almost identical (2.269 Å and 2.267 Å, respectively), which are the shortest among all calculated minerals. The variation of CaO content in pigeonite shows a small effect on the average Ca–O bond length, which slightly decreases from 2.375 Å to 2.361 Å when the CaO content decreases from 6.86 wt.% to 1.74 wt.%. The average Ca–O/S bond length increases in the order of forsterite < pigeonite < grossular < anorthite < oldhamite. Such a large variation in average Ca–O/S bond lengths suggests significant Ca isotope equilibrium fractionations among those Ca-bearing minerals.

Table 1
Fitting parameters of calculated reduced partition function ratios of $^{44}Ca/^{40}Ca$ ($10^3 \ln\beta$), average bond Ca–O/S lengths with a cutoff of 3.0 Å, and the CNs. Fitting equation: $1000\ln\beta = ax^3 + bx^2 + cx$, where $x = 10^6/T^2$, T is temperature in Kelvin. The temperature range for fitting is 275–2275 K.

Minerals	Formulae	a	b	c	Bond length (Å)	CN
Anorthite	$CaAl_2Si_2O_8$	6.21×10^{-5}	-5.68×10^{-3}	1.307	2.455	6.75
Forsterite	$Ca_{1/16}Mg_{31/16}SiO_4$	1.63×10^{-4}	-1.51×10^{-2}	2.355	2.269	6
Forsterite	$Ca_{1/32}Mg_{63/32}SiO_4$	0	0	2.362	2.267	6
Grossular	$Ca_3Al_2(SiO_4)_3$	1.08×10^{-4}	-1.08×10^{-2}	2.025	2.393	8
Oldhamite	CaS	4.89×10^{-6}	-1.71×10^{-3}	0.957	2.826	6
Pigeonite	$Ca_{1/8}Mg_{7/8}SiO_3$	1.15×10^{-4}	-1.11×10^{-2}	1.942	2.375	7
Pigeonite	$Ca_{2/32}Mg_{30/32}SiO_3$	0	0	1.964	2.373	7
Pigeonite	$Ca_{1/32}Mg_{31/32}SiO_3$	0	0	2.097	2.361	7
Orthopyroxene*	$Ca_{1/48}Mg_{47/48}SiO_3$	1.94×10^{-4}	-1.32×10^{-2}	2.104	2.300	6
Diopside*	$CaMgSi_2O_6$	1.18×10^{-4}	-6.89×10^{-3}	1.458	2.470	8

Data sources: *, Wang et al. (2017b).

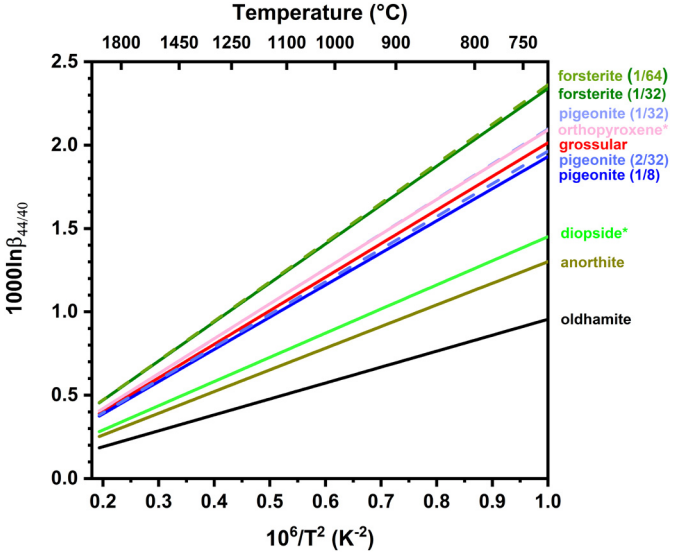

Fig. 2. The calculated $10^3 \ln\beta_{44/40}$ for anorthite, forsterite, grossular, oldhamite, and pigeonite at volumes corresponding to zero pressure using the static first-principles calculation. $10^3 \ln\beta_{44/40}$ for diopside and orthopyroxene are from Wang et al. (2017b) in which the same calculation method was employed. (For interpretation of the colors in the figure(s), the reader is referred to the web version of this article.)

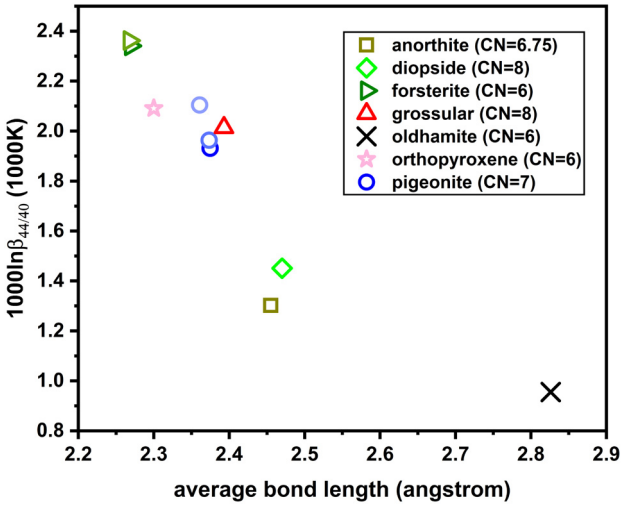

Fig. 3. Negative correlation between $10^3 \ln\beta_{44/40}$ at 1000 K and the average Ca–O/S bond lengths.

3.3. Calculated Ca isotope fractionation factors

The RPFR ($10^3 \ln\beta$) of $^{44}Ca/^{40}Ca$ ratios are shown in Fig. 2 and their polynomial fitting parameters with the temperature from 275 K to 2275 K are given in Table 1. Combining our previous studies (Wang et al., 2017b) and current calculations, we find that the enrichment of heavy Ca isotopes follows the order of forsterite > opx > grossular ~ pigeonite > diopside > anorthite > oldhamite, suggesting large equilibrium fractionations of Ca isotope among these common Ca-bearing minerals even at high temperature. For example, the equilibrium isotope fractionation ($10^3 \ln\alpha$) of $^{44/40}Ca$ between forsterite and oldhamite at 1000 K is up to 1.4‰.

4. Discussion

4.1. Effect of crystal structure and concentration on Ca isotope fractionation

In general, the $10^3 \ln\beta$ of an element are controlled by the bond strengths, which are significantly affected by oxidation states, electronic configurations, and the local crystal structures of minerals such as the CN (Schauble, 2004). Generally, shorter chemical bonds correspond to stronger bond strengths and have higher vibrational frequencies, which result in the enrichment in heavier isotopes relative to longer chemical bonds (Urey, 1947; Schauble, 2004; Hill and Schauble, 2008; Young et al., 2009; Wang et al., 2017a, 2017b). Our results suggest that the variation in $10^3 \ln\beta$ of $^{44}Ca/^{40}Ca$ of the calculated minerals is also mainly ascribed to the difference in the local structure. Overall, minerals with shorter bond lengths are more enriched in heavy Ca isotopes than those with longer bonds (Fig. 3).

Previous studies (Feng et al., 2014; Wang et al., 2017a, 2017b) suggested that the variation in chemical compositions (such as Mg or Ca content) at a certain range shows a significant effect on $10^3 \ln\beta$ (or $10^3 \ln\alpha$), which is corresponding to the variation of the bond lengths. For instance, $10^3 \ln\alpha$ of $^{44}Ca/^{40}Ca$ between opx and diopside increases significantly from 0.14‰ to 0.64‰ at 1000 K when the CaO content in opx decreases from 6.84 wt.% to 1.16 wt.%, but it almost remains constant when the CaO content is lower than 1.16 wt%, showing a good linear correlation with their average Ca–O bond lengths (Fig. 5a in Wang et al., 2017b). As two solid solutions, Ca-bearing forsterite and pigeonite have variable Ca contents. Here we also performed theoretical calculations to investigate the Ca concentration effect on $10^3 \ln\beta$ of $^{44}Ca/^{40}Ca$ of forsterite and pigeonite. Our results show that both the average Ca–O bond lengths and $10^3 \ln\beta$ of $^{44}Ca/^{40}Ca$ of forsterite with 2.48 wt.% and 1.25 wt.% CaO are almost identical (Table 1 and Fig. 4), suggesting that the CaO content of 2.48 wt.% is a threshold below which the Ca concentration effect is negligible. For pigeonite, $10^3 \ln\beta$ of $^{44}Ca/^{40}Ca$ at 1000 K slightly increases from 1.931‰ to 2.097‰ when the CaO content decreases from

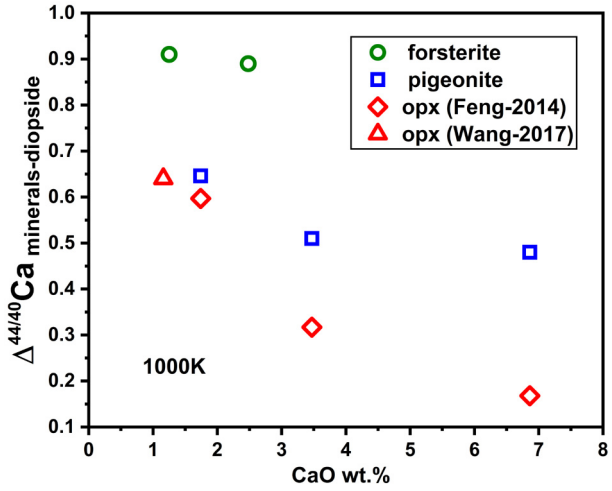

Fig. 4. Effects of Ca concentration on Ca isotope fractionation at 1000 K for forsterite, pigeonite, and enstatite. The intervals, where Ca isotope fractionation shows significant concentration effect, are similar for pigeonite and enstatite.

6.86 wt.% to 1.74 wt.% and average Ca–O bond length increases from 2.361 Å to 2.375 Å, indicating a mild effect of Ca concentration on $10^3 \ln\beta$ (Table 1 and Fig. 4).

4.2. Constraints on the origin of oldhamite in enstatite chondrites

Enstatite chondrites are the isotopically closest meteorites to the Earth for many elements, including O, Ca, Ti, Cr, and Ni (e.g., Clayton, 2003; Huang and Jacobsen, 2017; Trinquier et al., 2009; Mougel et al., 2018; Regelous et al., 2008). They are therefore particularly important for understanding the chemical composition and evolution of the Earth. Enstatite chondrites are among the most reduced meteorites and contained some unusual sulfide minerals such as oldhamite (CaS) in which about half of the Ca in the enstatite chondrite Indarch is stored (Valdes et al., 2014). Some previous studies (e.g., Gannoun et al., 2011; El Goresy et al., 2017) suggested that oldhamite may originate from nebular condensation according to thermodynamic calculations, their REEs patterns, and the intergrowth of minerals, while others argued that oldhamite are secondary products of parent body processes because of their igneous texture and the unique mineral inventories such as the coexistence of silica and sulfide (e.g., Lehner et al., 2013). There is a lack of efficient indicators that can distinguish these processes. For instance, REE enrichment in oldhamite can originate from either nebular condensation (Lodders and Fegley, 1993; Lodders, 1996) or complex igneous processes including fractional crystallization, subsolidus annealing and exsolution (Dickinson and McCoy, 1997). Here we show that the Ca isotopic composition of oldhamite provides a useful way to constrain its formation process.

4.2.1. Formation of CaS by silicate sulfidation?

Lehner et al. (2013) investigated petrography and mineral chemistry of EH3 chondrites and proposed that sulfides (e.g., FeS, CaS, and MgS) formed from the sulfidation of FeO-bearing silicates during igneous processes. Such an open-system interaction between silicates and a S-rich gas can explain the mineral inventories, such as the association of silica with abundant niningerite (MgS) and troilite (FeS) in the EH3 chondrites, as well as their low bulk Mg/Si ratios. This implies that the oldhamite (CaS) could form via the reaction:

$$\mathrm{Ca}_x\mathrm{Mg}_{(2-x)}\mathrm{Si}_2\mathrm{O}_6(s) + \mathrm{S}_2(g) = x\mathrm{CaS}(s) + (2-x)\mathrm{MgS}(s) + 2\mathrm{SiO}_2(s) + \mathrm{O}_2(g) \quad (2)$$

If the Ca-bearing pyroxene is exhausted, the product CaS will inherit the REE and Ca isotopic compositions from the pyroxene. Otherwise, the REE and Ca isotopes will be redistributed between CaS and pyroxene during the reaction. In the latter case, CaS should be enriched in lighter Ca isotopes relative to the coexisting silicates because CaS has the lowest $10^3 \ln\beta_{44/40}$ among all calculated minerals (Table 1 and Fig. 2). However, Valdes et al. (2014) found that the $\delta^{44/40}$Ca of CaS in the Indarch enstatite chondrites (EH4) is higher than the silicate portion by at least 0.36‰, arguing against formation of CaS by the silicate sulfidation.

4.2.2. Nebular gas condensation

The condensation of solar nebular gas in reducing environment has been regarded as a possible mechanism for the formation of oldhamite in enstatite chondrites (e.g., Herndon and Suess, 1976; Yokoyama et al., 2017). The β factor of a mineral can be regarded as the equilibrium fractionation factor of Ca isotopes between this mineral and vapor. Thus, condensed Ca-bearing minerals from nebular gas are enriched in heavy Ca isotopes relative to the residual gaseous Ca because β-factor values are greater than unity. Previous theoretical studies based on thermodynamic calculations on enstatite chondrites suggested that oldhamite is one of the early Ca-bearing minerals condensing from nebular gas, while anorthite and diopside may form from later reactions between CaS and isotopically light gas at slightly lower temperature (Lodders and Fegley, 1993). If so, the silicate phases in enstatite chondrites should be enriched in the lighter Ca isotopes compared to oldhamite. Therefore, the condensation of oldhamite prior to other Ca-bearing minerals can well support the observed enrichment of heavy Ca isotopes in oldhamite relative to the coexisting silicate portion (Valdes et al., 2014).

4.3. Heterogeneous Ca isotopic composition in the Moon?

It is widely accepted that the Moon formed from the giant impact between the proto-Earth and an impactor, named Theia, and underwent the solidification and differentiation of the LMO (e.g., Canup, 2004, 2012; Ćuk and Stewart, 2012; Warren, 1985; Snyder et al., 1992). Here we will show that the calcium isotopic compositions of lunar rocks can be used to test different models of Moon formation and the differentiation of the LMO. From the surface of the Earth and Moon to depth, the major Ca-bearing phases gradually change from plagioclase + cpx to garnet + cpx. Due to the large equilibrium Ca isotope fractionations among those Ca-bearing minerals, it is likely that mineral crystallizations from the LMO have produced Ca isotope heterogeneity. Although the primordial Ca isotope heterogeneity in the Earth disappeared due to intensive mantle convection, such signatures could be well preserved in the solid Moon due to the lack of plate tectonics (Head and Solomon, 1981), which can thus be used to constrain the evolution of the Moon.

On the basis of our calculations, we simulated the evolution of the Ca isotopic composition during the crystallization of the LMO. Although there are different solidification processes in different LMO models due to the distinct initial settings of the major and trace elements, the general trends for crystallization of Ca-bearing minerals are similar (Snyder et al., 1992; Elkins-Tanton et al., 2011; Elardo et al., 2011; Lin et al., 2017) and the first-order estimation of Ca isotopic variations does not depend on the selected LMO models. For instance, according to Elkins-Tanton et al. (2011), the solidification process of the Moon can be divided into four stages: (1) 100% olivine, (2) 90% orthopyroxene + 10% olivine, (3) 20% olivine + 10% orthopyroxene + 20% pigeonite + 50% plagioclase, and (4) 30% orthopyroxene + 20% clinopyroxene + 40% plagioclase + 10% oxides. The temperature gradient of the LMO is assumed to

follow the solidus of the residual magma used in Elkins-Tanton et al. (2011):

$$T(r) = -1.3714*r^2/10^4 - 0.1724*r + 1861 - \frac{4.4}{0.2*L+0.01} \quad (3)$$

where r is the radius in km and L is the residual magma fraction.

Based on the calculated fractionation factors in this study and the LMO solidification models, we estimated the Ca isotopic fractionation during the evolution of the LMO. For simplicity, density differences among all phases under different temperatures and pressures are neglected which means that mass fraction of the minerals can be converted to volume fractions. In each stage, according to the mass balance of ^{40}Ca and ^{44}Ca, we have

$$d(F*[^{40}\mathrm{Ca}]) = (K_{D40}*[^{40}\mathrm{Ca}] + w_{40})*dF \quad (4)$$

$$d(F*[^{44}\mathrm{Ca}]) = (K_{D44}*[^{44}\mathrm{Ca}] + w_{44})*dF \quad (5)$$

where $[^{40}\mathrm{Ca}]$ and $[^{44}\mathrm{Ca}]$ are mass fractions of Ca isotopes in the melt, K_{D40} and K_{D44} are bulk partition coefficients of ^{40}Ca and ^{44}Ca between solid phases (excluding diopside or anorthite) and melt, w_{40} and w_{44} are mass fractions of ^{40}Ca and ^{44}Ca in the cumulate from diopside (and/or anorthite), respectively, and F is the remaining liquid fraction relative to the initial value in each stage. For example, during the third stage of the solidification process where the cumulate consists of olivine, opx, pigeonite, plagioclase, and melt, we obtain

$$\begin{aligned} K_{D40} &= P_{melt}\times K_{D40,melt} \\ &\quad + P_{forsterite}\times K_{D40,forsterite} + P_{enstatite}\times K_{D40,enstatite} \\ &\quad + P_{pigeonite}\times K_{D40,pigeonite} \end{aligned} \quad (6)$$

$$\begin{aligned} K_{D44} &= P_{melt}\times K_{D44,melt} \\ &\quad + P_{forsterite}\times K_{D44,forsterite} + P_{enstatite}\times K_{D44,enstatite} \\ &\quad + P_{pigeonite}\times K_{D44,pigeonite} \\ &= P_{melt}\times K_{D40,melt}\times\alpha_{melt} + P_{forsterite}\times K_{D40,forsterite} \\ &\quad \times\alpha_{forsterite} + P_{enstatite}\times K_{D40,enstatite}\times\alpha_{enstatite} \\ &\quad + P_{pigeonite}\times K_{D40,pigeonite}\times\alpha_{pigeonite} \end{aligned} \quad (7)$$

$$w_{40} = P_{anorthite}\times w_{anorthite} \quad (8)$$

$$w_{44} = P_{anorthite}\times w_{anorthite}\times\alpha_{pigeonite}\times([^{40}\mathrm{Ca}]/[^{44}\mathrm{Ca}]) \quad (9)$$

where 'P' is the mass weight of mineral or melt in the cumulate, 'K_D' is the partition coefficient between minerals and melt, 'α' is the equilibrium Ca isotope fractionation factor between minerals and melt, and 'w' is the mass fraction of Ca in minerals in which Ca is the major element such as diopside and anorthite. The parameters used for modeling are listed in Table S6.

Because diopside is the main reservoir of Ca among solid phases during partial melting of the mantle, we assume that $\Delta^{44/40}$Ca between diopside and melt is 0 ± 0.05‰ at 1000 K (Qi et al., 2017), which can be further used to estimate equilibrium fractionation between melt and other Ca-bearing minerals (Fig. 5). Temperatures for the mineral crystallization at different depths are obtained from Eq. (3). Plagioclase floats upward to the Moon's surface forming anorthosite layer, while other minerals are crystallized from the bottom of the LMO (e.g. Wood et al., 1970; Warren, 1985; Suckale et al., 2012).

Equations (4) and (5) were solved sequentially with the parameters listed in Table 1 and Table S6 to obtain an integral picture about the Ca isotopic evolution and distribution in the solidified LMO (see animation 1 and the Matlab code in Supplementary Materials for details). As the solidification proceeds, $\delta^{44/40}$Ca of olivine and opx that cumulate at the bottom of the LMO is higher than the initial Ca isotopic composition by 0.17 to 0.26‰ (Fig. 6) because olivine and opx are enriched in heavy Ca isotopes relative to the melt. Despite of up to 80% of crystallization, $\delta^{44/40}$Ca of the remaining melt only changes by less than 0.05‰ due to the low Ca content in olivine-opx cumulate (about 16% Ca of the whole LMO). After this stage, plagioclase crystallizes with the enrichment of light Ca isotopes relative to the coexisting melt. Because of their low density, plagioclases float to the top of the LMO forming the anorthositic crust. Although the mafic cumulate at the bottom is enriched in heavy Ca isotopes, $\delta^{44/40}$Ca of the remaining melt only increases slightly because plagioclase has a much higher Ca content than the mafic minerals except cpx which has a similar Ca isotopic composition to the melt (Qi et al., 2017). The simulation

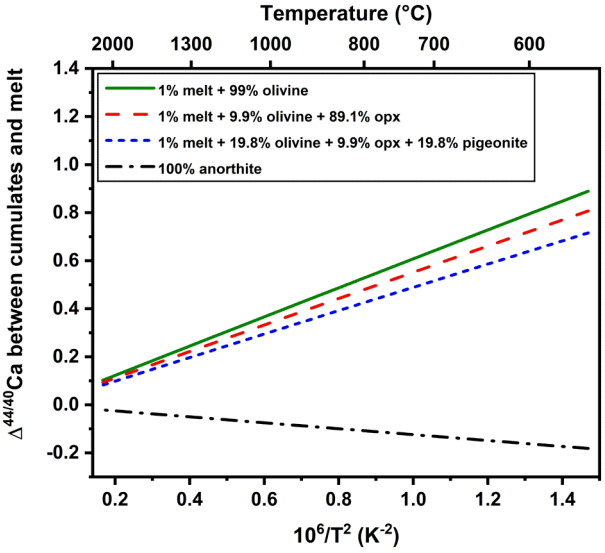

Fig. 5. Equilibrium Ca isotope fractionation between melt and cumulates, of which crystallizing assemblages vary during the solidification process of the LMO (Table S5). 1% of interstitial melt is considered in cumulates. The partition coefficients of Ca between minerals and melt for olivine, opx, and pigeonite are approximately set to 0.02, 0.12, and 0.6 respectively.

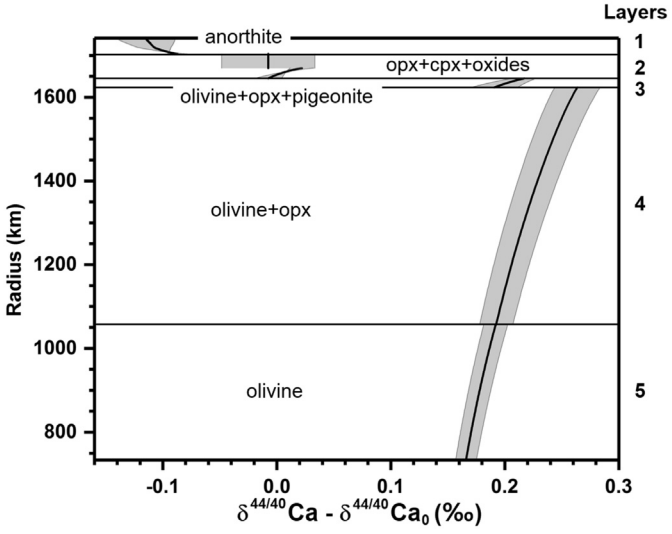

Fig. 6. Calcium isotopic fractionation ($\delta^{44/40}$Ca–$\delta^{44/40}$Ca$_0$) of the crystallized LMO before overturning. $\delta^{44/40}$Ca$_0$ is the initial Ca isotope composition of the LMO. The lunar mantle is divided into 5 layers with different mineral assemblages. Simulation stops when the fraction of residual melt is less than 6% where the content of Ca in the melt sharply decreases due to crystallization of plagioclase and cpx, as shown with a vertical line in $\delta^{44/40}$Ca in the layer 2. The grey zone represents propagation error of $\delta^{44/40}$Ca assuming that the error for $\Delta^{44/40}$Ca$_{cumulate\text{-}melt}$ is ±0.05‰.

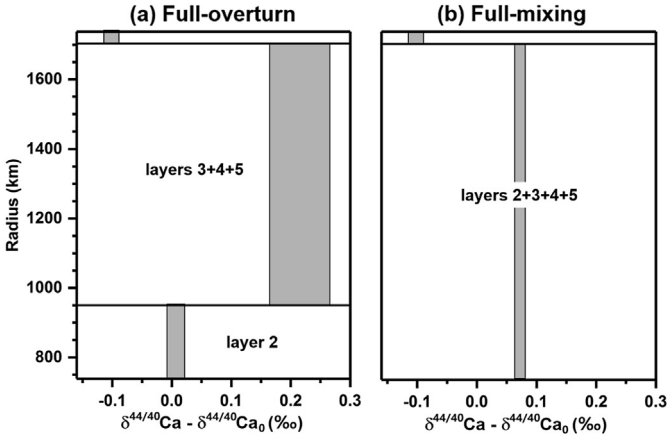

Fig. 7. Calcium isotopic fractionation ($\delta^{44/40}$Ca–$\delta^{44/40}$Ca$_0$) of the overturned lunar mantle. $\delta^{44/40}$Ca$_0$ is the initial Ca isotope composition of the LMO. Two extreme situations are shown: (a) full-overturn, layer 2 with oxides and higher density in sinks into the bottom of the LMO; (b) full-mixing, in which case layers below the buoyant anorthosite crust are well mixed and homogenized.

stops when the fraction of residual melt is less than 6%, where the Ca content of the melt sharply decreases due to the crystallization of plagioclase and cpx. Our models show that the final $\delta^{44/40}$Ca of the anorthositic crust is lower than the starting composition by 0.09 to 0.11‰, suggesting that the anorthositic crust is slightly enriched in light Ca isotopes relative to the bulk LMO (Fig. 6). This small offset can barely be resolved within the current analytical uncertainty (0.1–0.15‰). However, our models predict that the $\delta^{44/40}$Ca of the lunar mantle is higher than that of the anorthositic crust by 0.26 to 0.33‰, which is resolvable and could be tested in future studies.

We further investigated the gravitationally driven overturn of the lunar mantle, which may affect the structure and Ca isotopic composition of the lunar mantle. Two extreme situations are considered here, i.e., full overturn and full mixing. For the case of full overturn, the cumulate in layer 2 (cpx, opx, and oxide) sinks to the bottom of the LMO due to its higher density. The shallower lunar mantle (mixture of layer 3, 4, and 5) is mainly composed of olivine, opx, and pigeonite with $\delta^{44/40}$Ca 0.17–0.26‰ higher than the initial composition (Fig. 7a). If the lunar mantle is well mixed, its Ca isotopic composition is homogeneous, which is slightly heavier than the LMO by 0.06–0.08‰ based on the mass balance with the anorthositic crust (Fig. 7b). Therefore, regardless of the overturn process, the lunar mantle should have distinct Ca isotopic composition from that of the anorthositic crust. Although Ca isotope data of the Moon rocks and minerals are still rare (Simon and DePaolo, 2010; Valdes et al., 2014; Simon et al., 2017), and future analyses of lunar samples to determine the composition of the lunar mantle and of the anorthosites will allow to test the models of differentiation of the LMO.

5. Conclusions

Equilibrium Ca isotope fractionation factors of Ca-bearing minerals are investigated using first-principles calculations based on the DFT. The sequence of heavy Ca isotope enrichment is forsterite > orthopyroxene (opx) > grossular ∼ pigeonite > diopside > anorthite > oldhamite. Equilibrium Ca isotope fractionation factors are mainly controlled by the Ca–O bond lengths.

Our results show that under equilibrium oldhamite is enriched in light Ca isotopes relative to other Ca-bearing minerals. Given that oldhamites in the Indarch enstatite chondrite are isotopically heavier than the silicate phases, they should not be in isotopic equilibrium with the coexisting silicates. This implies that oldhamite should originate from the condensation of solar nebular gas, rather than being produced by igneous processes. Furthermore, our simulations for the solidification of the LMO predict that the average $\delta^{44/40}$Ca of the lunar anorthositic crust are lower than the bulk Moon by 0.1‰, while the lunar mantle could have higher $\delta^{44/40}$Ca than the bulk Moon by 0.17–0.26‰ if the mantle is overturned and stratified, or by 0.06–0.08‰ if the mantle is fully mixed and isotopically homogeneous. Therefore, Ca isotope data for lunar rocks can be used to test the solidification and evolution models of the LMO.

Acknowledgements

This study was supported by the Strategic Priority Research Program (B) of Chinese Academy of Sciences (Grant No. XDB18000000), National Science Foundation of China (41473011, 41173031, and 41325011). The computations were performed on the supercomputing system in the Supercomputing Center at the University of Science and Technology of China, Hefei, China. We thank Frederic Moynier for editorial handling and Merlin Méheut and three anonymous reviewers for constructive comments, which greatly improved the manuscript.

Appendix A. Supplementary material

Supplementary material related to this article can be found online at https://doi.org/10.1016/j.epsl.2018.12.034.

References

Amsellem, E., Moynier, F., Pringle, E.A., Bouvier, A., Chen, H., Day, J.M.D., 2017. Testing the chondrule-rich accretion model for planetary embryos using calcium isotopes. Earth Planet. Sci. Lett. 469, 75–83.

Avril, C., Malavergne, V., Caracas, R., Zanda, B., Reynard, B., Charon, E., Bobocioiu, E., Brunet, F., Borensztajn, S., Pont, S., Tarrida, M., 2013. Raman spectroscopic properties and Raman identification of CaS–MgS–MnS–FeS–Cr_2FeS_4 sulfides in meteorites and reduced sulfur-rich systems. Meteorit. Planet. Sci. 48 (8), 1415–1426.

Baroni, S., de Gironcoli, S., Dal Corso, A., Giannozzi, P., 2001. Phonons and related crystal properties from density-functional perturbation theory. Rev. Mod. Phys. 73 (2), 515–562.

Bigeleisen, J., Mayer, M.G., 1947. Calculation of equilibrium constants for isotopic exchange reactions. J. Chem. Phys. 15 (5), 261–267.

Canup, R.M., 2004. Simulations of a late lunar-forming impact. Icarus 168, 433–456.

Canup, R.M., 2012. Forming a Moon with an Earth-like composition via a giant impact. Science 338 (6110), 1052–1055.

Cao, X., Liu, Y., 2011. Equilibrium mass-dependent fractionation relationships for triple oxygen isotopes. Geochim. Cosmochim. Acta 75, 7435–7445.

Clayton, R.N., 2003. Oxygen isotopes in the Solar System. Space Sci. Rev. 106, 19–32.

Ćuk, M., Stewart, S.T., 2012. Making the Moon from a fast-spinning Earth: a giant impact followed by resonant despinning. Science 338 (6110), 1047–1052.

Dickinson, T.L., McCoy, T.J., 1997. Experimental rare-earth-element partitioning in oldhamite: implications for the igneous origin of aubritic oldhamite. Meteorit. Planet. Sci. 32 (3), 395–412.

Ducher, M., Blanchard, M., Balan, E., 2016. Equilibrium zinc isotope fractionation in Zn-bearing minerals from first-principles calculations. Chem. Geol. 443, 87–96.

Elardo, S.M., Draper, D.S., Shearer, C.K., 2011. Lunar Magma Ocean crystallization revisited: bulk composition, early cumulate mineralogy, and the source regions of the highlands Mg-suite. Geochim. Cosmochim. Acta 75, 3024–3045.

Elkins-Tanton, L.T., Burgess, S., Yin, Q., 2011. The lunar magma ocean: reconciling the solidification process with lunar petrology and geochronology. Earth Planet. Sci. Lett. 304 (3–4), 326–336.

Feng, C., Qin, T., Huang, S., Wu, Z., Huang, F., 2014. First-principles investigations of equilibrium Ca isotope fractionation between orthopyroxene and clinopyroxene. Geochim. Cosmochim. Acta 143, 132–142.

Fujii, T., Moynier, F., Dauphas, N., Abe, M., 2011. Theoretical and experimental investigation of nickel isotopic fractionation in species relevant to modern and ancient oceans. Geochim. Cosmochim. Acta 75, 469–482.

Fujii, T., Moynier, F., Blichert-Toft, J., Albarede, F., 2014. Density functional theory estimation of isotope fractionation of Fe, Ni, Cu, and Zn among species relevant to geochemical and biological environments. Geochim. Cosmochim. Acta 140, 553–576.

El Goresy, A., Lin, Y., Miyahara, M., Gannoun, A., Boyet, M., Ohtani, E., Gillet, P., Trieloff, M., Simionovici, A., Feng, L., Lemelle, L., 2017. Origin of EL 3 chondrites: evidence for variable C/O ratios during their course of formation—a state of the art scrutiny. Meteorit. Planet. Sci. 52 (5), 781–806.

Gannoun, A., Boyet, M., El Goresy, A., Devouard, B., 2011. REE and actinide microdistribution in Sahara 97072 and ALHA77295 EH3 chondrites: a combined cosmochemical and petrologic investigation. Geochim. Cosmochim. Acta 75 (11), 3269–3289.

Giannozzi, P., Baroni, S., Bonini, N., Calandra, M., Car, R., Cavazzoni, C., Ceresoli, D., Chiarotti, G.L., Cococcioni, M., Dabo, I., Dal Corso, A., de Gironcoli, S., Fabris, S., Fratesi, G., Gebauer, R., Gerstmann, U., Gougoussis, C., Kokalj, A., Lazzeri, M., Martin-Samos, L., Marzari, F., Mazzarello, R., Paolini, S., Pasquarello, A., Paulatto, L., Sbraccia, C., Scandolo, S., Sclauzero, G., Seitsonen, A.P., Smogunov, A., Umari, P., Wentzcovitch, R.M., 2009. QUANTUM ESPRESSO: a modular and open-source software project for quantum simulation of materials. J. Phys. Condens. Matter 21, 395502.

Head, J.W., Solomon, S.C., 1981. Tectonic evolution of the terrestrial planets. Science 213, 62–76.

Herndon, J.M., Suess, H.E., 1976. Can enstatite meteorites form from a nebula of solar composition? Geochim. Cosmochim. Acta 40, 395–399.

Hill, P.S., Schauble, E.A., 2008. Modeling the effects of bond environment on equilibrium iron isotope fractionation in ferric aquo-chloro complexes. Geochim. Cosmochim. Acta 72 (8), 1939–1958.

Huang, F., Chen, L., Wu, Z., Wang, W., 2013. First-principles calculations of equilibrium Mg isotope fractionations between garnet, clinopyroxene, orthopyroxene, and olivine: implications for Mg isotope thermometry. Earth Planet. Sci. Lett. 367, 61–70.

Huang, F., Wu, Z., Huang, S., Wu, F., 2014. First-principles calculations of equilibrium silicon isotope fractionation among mantle minerals. Geochim. Cosmochim. Acta 140, 509–520.

Huang, S., Jacobsen, S.B., 2017. Calcium isotopic compositions of chondrites. Geochim. Cosmochim. Acta 201, 364–367.

Huang, S., Farkas, J., Jacobsen, S.B., 2010. Calcium isotopic fractionation between clinopyroxene and orthopyroxene from mantle peridotites. Earth Planet. Sci. Lett. 291, 337–344.

Javoy, M., Kaminski, E., Guyot, F., Andrault, D., Sanloup, C., Moreira, M., Labrosse, S., Jambon, A., Agrinier, P., Davaille, A., Jaupart, C., 2010. The chemical composition of the Earth: enstatite chondrite models. Earth Planet. Sci. Lett. 293, 259–268.

Kang, J.-T., Zhu, H.-L., Liu, Y.-F., Liu, F., Wu, F., Hao, Y.-T., Zhi, X.-C., Zhang, Z.-F., Huang, F., 2016. Calcium isotopic composition of mantle xenoliths and minerals from Eastern China. Geochim. Cosmochim. Acta 174, 335–344.

Kang, J.-T., Ionov, Dmitri A., Liu, F., Zhang, C.-L., Golovine Alexander, V., Qin, L.-P., Zhang, Z.-F., Huang, F., 2017. Calcium isotopic fractionation in mantle peridotites by melting and metasomatism, and Ca isotope composition of Bulk Silicate Earth. Earth Planet. Sci. Lett. 474, 128–137.

Lajaeghere, K., Bihlmayer, G., Bjorkman, T., Blaha, P., Blugel, S., Blum, V., Caliste, D., Castelli, I.E., Clark, S.J., Corso, A.D., Gironcali, S., Deutsch, T., Dewhurst, J.K., Marco, I.D., Draxl, C., Dulak, M., Eriksson, O., Flores-Livas, J.A., Garrity, K.F., Genovese, L., Giannozzi, O., Guantomassi, N., Geiedecjerm, S., Gonze, X., Granas, O., Gross, E.K.U., Gulans, A., Gygi, F., Hamann, D.R., Hasnip, P.J., Holzwarth, A.A.W., Iusan, D., Jochym, D.B., Jollet, F., Jones, D., Kresse, G., Koepernik, K., Kucukbenli, E., Kvashnin, Y.O., Locht, I.L.M., Lubeck, S., Marsman, M., Marzari, N., Nitzsche, U., Nordstrom, L., Ozaki, T., Paulatto, L., Pickard, C.J., Peolmans, W., Probert, M.I.J., Refson, K., Richter, M., Rignanese, G., Saha, S., Scheffler, M., Schlipf, M., Schwarz, K., Sharma, S., Tavazza, F., Thunstrom, P., Tkatchenko, A., Torrent, M., Vanderbilt, D., Setten, M.J., Speyboeck, V.V., Wills, J.M., Yates, J.R., Zhang, G.-X., Cottenier, S., 2016. Reproducibility in density functional theory calculations of solids. Science 351, 1415.

Lehner, S.W., Petaev, M.I., Zolotov, M.Y., Buseck, P.R., 2013. Formation of niningerite by silicate sulfidation in EH3 enstatite chondrites. Geochim. Cosmochim. Acta 101, 34–56.

Lin, Y., Tronche, E.J., Steenstra, E.S., van Westrenen, W., 2017. Evidence for an early wet Moon from experimental crystallization of the lunar magma ocean. Nat. Geosci. 10, 14–18.

Lodders, K., 1996. An experimental and theoretical study of rare-earth-element partitioning between sulfides (FeS, CaS) and silicate and applications to enstatite achondrites. Meteorol. Planet. Sci. 31, 749–766.

Lodders, K., 2003. Solar system abundances and condensation temperatures of the elements. Astrophys. J. 591, 1220–1247.

Lodders, K., Fegley, B., 1993. Lanthanide and actinide chemistry at high C/O ratios in the solar nebula. Earth Planet. Sci. Lett. 117, 125–145.

Magna, T., Gussone, N., Mezger, K., 2015. The calcium isotope systematics of Mars. Earth Planet. Sci. Lett. 430, 86–94.

Méheut, M., Lazzeri, M., Balan, E., Mauri, F., 2009. Structural control over equilibrium silicon and oxygen isotopic fractionation: a first-principles density-functional theory study. Chem. Geol. 258, 28–37.

Méheut, M., Schauble, E.A., 2014. Silicon isotope fractionation in silicate minerals: insights from first-principles models of phyllosilicates, albite and pyrope. Geochim. Cosmochim. Acta 134, 137–154.

Mougel, B., Moynier, F., Gopel, C., 2018. Chromium isotopic homogeneity between the Moon, the Earth, and enstatite chondrites. Earth Planet. Sci. Lett. 481, 1–8.

Moynier, F., Fujii, T., 2017. Calcium isotope fractionation between aqueous compounds relevant to low-temperature geochemistry, biology and medicine. Sci. Rep. 7, 44255. https://doi.org/10.1038/srep44255.

Norman, M.D., Borg, L.E., Nyquist, L.E., Bogard, D.D., 2003. Chronology, geochemistry, and petrology of a ferroan noritic anorthosite clast from Descartes breccia 67215: clues to the age, origin, structure, and impact history of the lunar crust. Meteorol. Planet. Sci. 38, 645–661.

Perdew, J.P., Zunger, A., 1981. Self-interaction correction to density-functional approximations for many-electron systems. Phys. Rev. B 23 (10), 5048–5079.

Qi, Y.-H., Liu, X.-H., Kang, J.-T., He, L.-X., Huang, F., 2017. First-principles investigations of equilibrium Ca, Mg, Si and O isotope fractionations between silicate melts and minerals. In: AGU Fall Meeting. New Orleans, LA, 11–15 December. #V33C-0537.

Qin, T., Wu, F., Wu, Z., Huang, F., 2016. First-principles calculations of equilibrium fractionation of O and Si isotopes in quartz, albite, anorthite, and zircon. Contrib. Mineral. Petrol. 171 (11), 91.

Regelous, M., Elliott, T., Coath, C.D., 2008. Nickel isotope heterogeneity in the early solar system. Earth Planet. Sci. Lett. 272, 330–338.

Schauble, E.A., 2004. Applying stable isotope fractionation theory to new systems. Rev. Mineral. Geochem. 55, 65–111.

Schauble, E.A., 2011. First-principles estimates of equilibrium magnesium isotope fractionation in silicate, oxide, carbonate and hexaaquamagnesium (2+) crystals. Geochim. Cosmochim. Acta 75, 844–869.

Simon, J.I., DePaolo, D.J., 2010. Stable calcium isotopic composition of meteorites and rocky planets. Earth Planet. Sci. Lett. 289, 457–466.

Simon, J.I., Jordan, M.K., Tappa, M.J., Schauble, E.A., Kohl, I.E., Young, E.D., 2017. Calcium and titanium isotope fractionation in refractory inclusions: tracers of condensation and inheritance in the early solar protoplanetary disk. Earth Planet. Sci. Lett. 472, 277–288.

Snyder, G.A., Taylor, L.A., Neal, C.R., 1992. A chemical model for generating the sources of mare basalts: combined equilibrium and fractional crystallization of the lunar magmasphere. Geochim. Cosmochim. Acta 123, 302–321.

Suckale, J., Elkins-Tanton, L.T., Sethian, J.A., 2012. Crystals stirred up, 2: numerical insights into the formation of the earliest crust on the Moon. J. Geophys. Res., Planets 117 (E8).

Trinquier, A., Elliott, T., Ulfbeck, D., Coath, C., Krot, A.N., Bizzarro, M., 2009. Origin of nucleosynthetic isotope heterogeneity in the solar protoplanetary disk. Science 324, 374–376.

Urey, H.C., 1947. The thermodynamic properties of isotopic substances. J. Chem. Soc. (Lond.), 562–581.

Valdes, M.C., Moreira, M., Foriel, J., Moynier, F., 2014. The nature of Earth's building blocks as revealed by calcium isotopes. Earth Planet. Sci. Lett. 394, 135–145.

Vanderbilt, D., 1990. Soft self-consistent pseudopotentials in a generalized eigenvalue formalism. Phys. Rev. B 41 (11), 7892–7895.

Wang, W.-Z., Qin, T., Zhou, C., Huang, S., Wu, Z., Huang, F., 2017a. Concentration effect on equilibrium fractionation of Mg–Ca isotopes in carbonate minerals: insights from first-principles calculations. Geochim. Cosmochim. Acta 208, 185–197.

Wang, W.-Z., Zhou, C., Qin, T., Kang, J.-T., Huang, S.-C., Wu, Z.-Q., Huang, F., 2017b. Effect of Ca content on equilibrium Ca isotope fractionation between orthopyroxene and clinopyroxene. Geochim. Cosmochim. Acta 219, 44–56.

Warren, P.H., 1985. The magma ocean concept and lunar evolution. Annu. Rev. Earth Planet. Sci. 13 (1), 201–240.

Wentzcovitch, R.M., 1991. Invariant molecular-dynamics approach to structural phase-transitions. Phys. Rev. B 44 (5), 2358–2361.

Wentzcovitch, R.M., Yu, Y.G., Wu, Z., 2010. Thermodynamic properties and phase relations in mantle minerals investigated by first principles quasiharmonic theory. Rev. Mineral. Geochem. 71 (1), 59–98.

Wood, J.A., Dickey, J.S., Marvin, U.B., Powell, B.N., 1970. Lunar anorthosites. Science 167 (3918), 602–604.

Yokoyama, K., Kimura, Y., Kaito, C., 2017. Experiments on condensation of calcium sulfide grains to demarcate environments for the formation of enstatite chondrites. ACS Earth Space Chem. 1, 601–607.

Young, E.D., Tonui, E., Manning, C.E., Schauble, E., Macris, C.A., 2009. Spinel–olivine magnesium isotope thermometry in the mantle and implications for the Mg isotopic composition of Earth. Earth Planet. Sci. Lett. 288 (3), 524–533.

Zhao, X., Zhang, Z., Huang, S., Liu, Y., Li, X., Zhang, H., 2017. Coupled extremely light Ca and Fe isotopes in peridotites. Geochim. Cosmochim. Acta 208, 368–380.